Materials Advances

ROYAL SOCIETY OF CHEMISTRY

PAPER

View Article Online
View Journal | View Issue

Check for updates

Cite this: *Mater. Adv.*, 2021, 2, 3685

Elucidating the role of non-covalent interactions in unexpectedly high and selective CO_2 uptake and catalytic conversion of porphyrin-based ionic organic polymers†

Sinem T. Kostakoğlu,[a] Yurii Chumakov,[bc] Yunus Zorlu,[a] Ali E. Sadak,[d] Serpil Denizaltı,[e] Ayşe G. Gürek[a] and Mehmet M. Ayhan*[a]

Received 11th March 2021,
Accepted 11th April 2021

DOI: 10.1039/d1ma00217a

rsc.li/materials-advances

Here, we present viologen-porphyrin based ionic covalent organic polymers (**H2-ICOP** and **Zn-ICOP**) with multiple CO_2-philic sites. The specific surface areas of **H2-ICOP** and **Zn-ICOP** were found to be 9 m^2 g^{-1} and 20 m^2 g^{-1}, respectively. CO_2 uptake analyses reveal that **H2-ICOP** exhibits very high CO_2 capture uptake (62.9 mg g^{-1}), which is one of the highest values among previously reported ICOPs. The results indicate very efficient non-covalent interactions between **H2-ICOP** and CO_2. The possible non-covalent interactions of hydrogen ($O_{CO_2}\cdots H-N$), tetrel ($C_{CO_2}\cdots N$, $C_{CO_2}\cdots Cl^-$), pnicogen ($O_{CO_2}\cdots N^+$), and spodium bonds ($O_{CO_2}\cdots Zn$) between CO_2 and **H2-ICOP** and **Zn-ICOP** are investigated *via* symmetry adapted perturbation theory (SAPT) analysis and electrostatic potential maps (MEP). The strength of non-covalent interactions in **H2-ICOP** and **Zn-ICOP** is decreasing in the following order $\Delta E_{C\cdots N} > \Delta E_{C\cdots Cl^-} > \Delta E_{O\cdots N^+}$ and $\Delta E_{Zn\cdots O} > \Delta E_{C\cdots Cl^-} > \Delta E_{C\cdots N} > \Delta E_{O\cdots N^+}$, respectively. The major CO_2 uptake contribution comes from $C_{CO_2}\cdots N$ tetrel bonding (−22.02 kJ mol^{-1}) interactions for **H2-ICOP**, whereas $O_{CO_2}\cdots Zn$ spodium bonding (−21.065 kJ mol^{-1}) interactions for **Zn-ICOP**. **H2-ICOP** has more CO_2-philic moieties with powerful non-covalent interactions compared to **Zn-ICOP**, which is in good agreement with the experimental results. Furthermore, the CO_2 catalytic conversion performances of **Zn-ICOP** and **H2-ICOP** gave good yields of 83% and 54%, respectively. Surprisingly, **Zn-ICOP**, despite having significantly lower CO_2 uptake capacity, displayed better catalytic activity than **H2-ICOP**, owing to a higher number of counter anions (Cl^-) on its surface, which shows the crucial role of the counter anion (Cl^-) in the mechanism of this catalytic reaction.

1. Introduction

The rise of the atmospheric carbon dioxide (CO_2) concentration has become a widespread concern due to its link to the greenhouse effect and threat to the environment.[1] Therefore, viable solutions for efficient capture and utilization of CO_2 (CCU) have received much attention in the past decades.[2,3] Among various CO_2 removal technologies, physical adsorbents such as zeolites, metal–organic frameworks (MOFs), covalent organic frameworks (COFs) and porous covalent organic polymers (COPs) came into focus owing to their high CO_2 capture capacities, catalytic transformation, and low energy requirements for regeneration.[4–8] Especially COPs have evolved for CCU due to their high specific surface areas, easily tunable pore structures, good chemical and thermal stabilities, tailored surface manipulation with polar groups, and variation in the synthesis.[9–13]

A high selective uptake of CO_2 is known to arise from large surface areas and non-covalent interactions between CO_2 and surfaces of materials. In the past decade, significant effort has been mainly focused on increasing the surface areas of materials and the non-covalent interactions between CO_2 and surfaces of materials have not attracted enough attention.[14] One should note that a large surface area is one of the parameters, but not the only one, that allows for high CO_2 capture. However, materials with a low surface area may still exhibit large CO_2 capture capacity with efficient non-covalent interactions with CO_2. Therefore, it is vitally important to identify and estimate the strength of these non-covalent interactions in terms of the contribution to the

[a] Gebze Technical University, Department of Chemistry, Kocaeli, 41400, Turkey. E-mail: menafayhan@gtu.edu.tr
[b] Gebze Technical University, Department of Physics, Kocaeli, 41400, Turkey
[c] Institute of Applied Physics, MD-2028, Chisinau, Moldova
[d] TUBITAK UME, Chemistry Group Laboratories, TR-41470, Gebze-Kocaeli, Turkey
[e] Ege University, Department of Chemistry, Bornova, İzmir, Turkey

† Electronic supplementary information (ESI) available: Synthesis and analysis details; photographs of gel-like or powder ICOPs; FTIR of **H2-ICOP-dx** and **Zn-ICOP-dx**; CP/MAS ^{13}C-NMR; PXRD with simulated patterns, EDS, DLS and zeta potentials for **H2-ICOP** and **Zn-ICOP**; SEM images of **H2-ICOP-dx** and **Zn-ICOP-dx**; formation of simultaneous tetrel bonds in **H2-ICOP** and **Zn-ICOP**; SAPT results for the interaction between two CO_2 molecules placed at the same porphyrin fragments in **H2-ICOP** and **Zn-ICOP**. See DOI: 10.1039/d1ma00217a

CO_2 capture capacity.[15,16] CO_2 is known to be able to form simultaneous non-covalent interactions *via* its electron-rich terminal oxygen atoms and its electron-deficient central carbon atom.[16,17] The electron-deficient central carbon atom acts as a Lewis acid (LA) and can form tetrel bonding interactions with anions or lone-pair-possessing atoms such as N, O, S, and F.[18–21] On the other hand, the electron-rich terminal oxygen atom acts as a Lewis base (LB) and can form hydrogen bonding with hydrogen atoms and, as recently reported, halogen bonding with halogen atom (I, Br, Cl) containing moieties.[22–29]

In particular, electron-rich nitrogen-based functional groups, such as amines, triazoles, triazine cores, imines, tetrazoles, benzimidazoles, azo linkages, and viologens, continue to be a dominant polar functional group to enhance the CO_2 adsorption capacity and CO_2/N_2 selectivity thanks to their multiple non-covalent interactions with CO_2.[20,27,30–38] Among nitrogen based adsorbents, viologen linked ionic covalent organic polymers (ICOPs) are of particular importance in CCU technologies because they not only have all the advantages of COPs but also possess charged cationic skeletons paired with counter-ions which provide additional CO_2 affinity owing to their electrostatic interactions with CO_2 molecules.[35,39–42] Consequently, the CO_2 uptake capacity of viologen linked ICOPs is found to be significantly higher compared to their neutral counterparts.[34,43,44] Moreover, unlike other porous materials, selective recognition of viologen linked ICOPs can be manipulated by simply controlling the redox state of viologen or the nature of the counter-ions for the desired application.[39,41]

In recent years, several cationic viologen linked ICOPs with good surface areas have been reported for CCU.[34,39,43–49] The general understanding of these studies is that the high CO_2 capture capacity of viologen linked ICOPs is credited mostly to tetrel bonding interactions between the counter anions and CO_2.[50] Commonly, nitrogen-based groups in CCU applications are preferred for their Lewis basic character to form non-covalent interactions with the electron-deficient central carbon (Lewis acid) of CO_2. However, in the case of viologen, the quaternary nitrogen (N^+) atom lacks lone electron pairs, and hence acts as a Lewis acid; consequently, the formation of efficient interactions between cation (N^+) nitrogen and the electron-rich terminal oxygen atoms of CO_2, commonly referred to as pnicogen bonds, is highly possible.[19,51] Yet, the pnicogen ($O_{CO_2}\cdots N^+$) interaction is often disregarded, and its contribution to CO_2 capture has not been reported.

However, despite their attractive features for CCU applications, only a limited number of viologen linked ICOPs have been reported in the literature, mainly due to their low physicochemical stability. This drawback can be overcome by the incorporation of viologens into polymeric systems with suitable rigid and symmetric macrocycles such as porphyrin.[52] The incorporation of porphyrin brings three advantages. First, unstable cationic species get stabilized by extended delocalized polymeric structures. Second, porphyrin is another excellent N containing molecular building block, which can increase the CO_2 uptake and selectivity through the CO_2 interaction with pyrroles (–C═N, –NH). Third, the metalation of the porphyrin core with Lewis acid metals such as zinc(II) can promote additional non-covalent interactions with the electron-rich terminal oxygen atoms of CO_2, known as spodium bonding.[53] In addition to their multiple CO_2-philic functional sides, both viologen and porphyrin are also known to exhibit effective CO_2 catalytic conversion, which makes them very promising bifunctional materials in CCU applications.[46–48,54–56]

Herein, based on the above considerations, we report viologen-linked porphyrin ICOPs (**H2-ICOP** and **Zn-ICOP**) synthesized through the Zincke reaction of H2 and Zn(II) tetrakis(4-aminophenyl) porphyrin with viologen Zincke salt, as presented in Scheme 1.

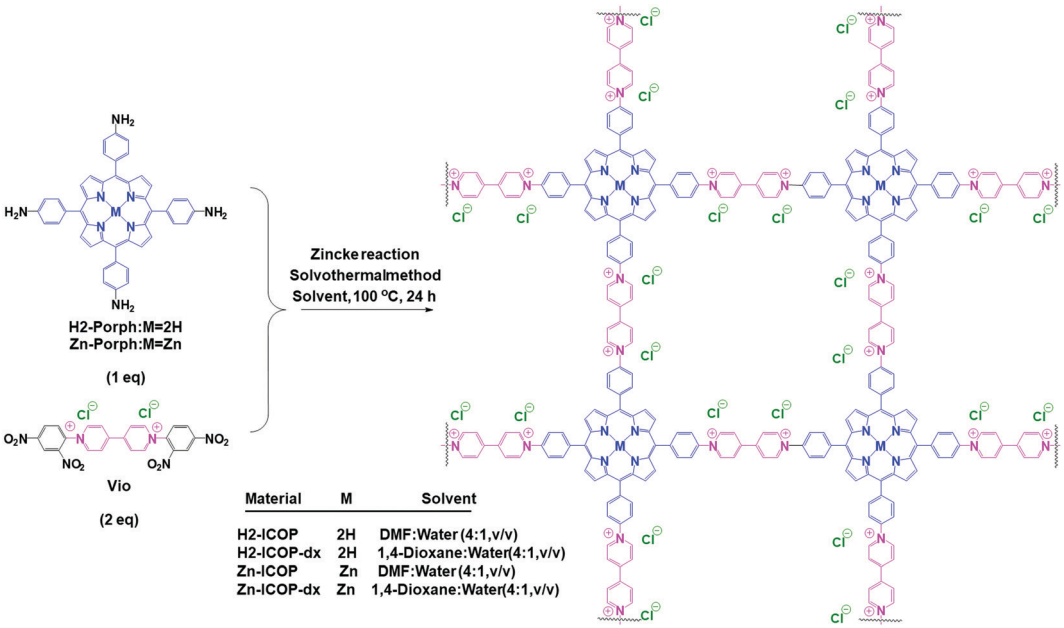

Scheme 1 Schematic representation of the synthesis of the viologen-linked porphyrin ICOPs *via* a Zincke reaction under solvothermal conditions.

The resultant ICOPs were characterized with various experimental analyses including FTIR spectroscopy, solid-state ^{13}C NMR spectroscopy, energy-dispersive X-ray spectroscopy (EDX), diffuse reflectance spectroscopy (DRS), thermogravimetric analysis (TGA), powder X-ray diffraction (PXRD), field emission scanning electron microscopy (SEM), transmission electron microscopy (TEM) and dynamic light scattering (DLS). Furthermore, their CO_2 capture capacity, CO_2/N_2 selectivity, and CO_2 catalytic conversion performances were explored. Brunauer–Emmett–Teller (BET) surface area analyses reveal that both **H2-ICOP** (9 $m^2\ g^{-1}$) and **Zn-ICOP** (20 $m^2\ g^{-1}$) possess very low surface areas. Yet, despite their nearly non-porous surfaces, especially **H2-ICOP** exhibits a very large CO_2 capture capacity (62.9 mg g^{-1}) and CO_2/N_2 selectivity, which indicates powerful non-covalent interactions with CO_2. Detailed theoretical analyses have been conducted to decode insights into these unexpected large CO_2 capture capacities and CO_2/N_2 selectivity. The strengths of possible non-covalent interactions, such as hydrogen, tetrel, pnicogen, and spodium bonding, between CO_2 molecules and the **H2-ICOP** and **Zn-ICOP** surfaces were calculated, in terms of the contribution to the CO_2 capture capacity. Additionally, the CO_2 catalytic conversion performances of **Zn-ICOP** and **H2-ICOP** gave good yields of 83% and 54% in mild conditions, respectively.

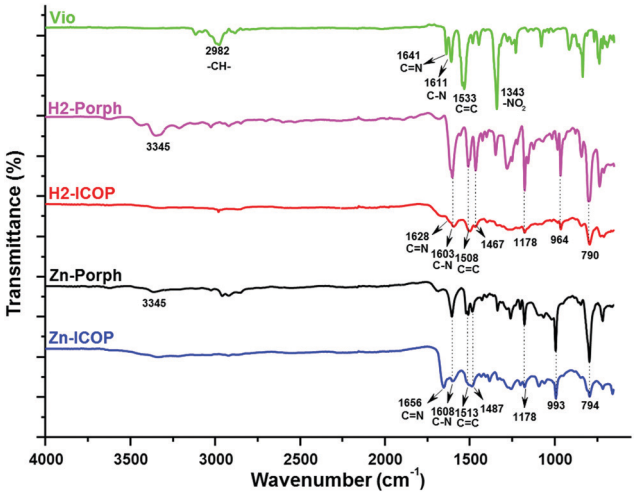

Fig. 1 FTIR spectra of **H2-ICOP** and **Zn-ICOP** in comparison with the corresponding monomers (**H2-Porph**, **Zn-Porph** and **Vio**).

2. Results and discussion

2.1. Synthesis and characterization

The synthesis of the ionic covalent organic polymers (**H2-ICOP** and **Zn-ICOP**) was carried out under solvothermal conditions by the Zincke reaction of 1,1′-bis(2,4-dinitrophenyl)-[4,4′-bipyridine]-1,1′-diium dichloride (**Vio**) with either 5,10,15,20-tetrakis(4-aminophenyl)porphyrin (**H2-Porph**) or 5,10,15,20-tetrakis(4-aminophenyl)porphyrinato zinc(II) (**Zn-Porph**) in a mixture of 1,4-dioxane : water (4 : 1, v/v) or DMF : water (4 : 1, v/v) (Scheme 1, for details see the ESI†). A gel-like material was obtained in the DMF : water mixture, whereas a powder was obtained in the 1,4-dioxane : water mixture (Fig. S1, ESI†). Washing the solids with the appropriate solvents is found to be crucial to remove unreacted starting materials and any smaller oligomers that may have formed. Therefore, the solids were washed with ethanol and DMSO several times until a colourless solution was obtained. The purification procedure was completed by washing with water and acetone. Complementary methods were used for the detailed structural characterization of the ICOPs. The formation of the ICOPs is confirmed by Fourier-transform infrared (FTIR) spectroscopy and solid-state ^{13}C NMR. In FTIR (Fig. 1), the decline of the characteristic $-NH_2$ peak at 3345 cm^{-1} and $-NO_2$ peak at 1343 cm^{-1} and the appearance of the characteristic pyridinium C═N peak at 1628 cm^{-1} for **H2-ICOP** and 1656 cm^{-1} for **Zn-ICOP** indicate the loss of the 2,4-dinitroaniline group and the formation of viologen-linked ICOPs. Besides, the peaks belonging to the porphyrin ring at 964 and 790 cm^{-1} for **H2-ICOP** and at 993 and 794 cm^{-1} for **Zn-ICOP** confirm the formation of the expected materials. The same structures are obtained for **H2-ICOP-dx** and **Zn-ICOP-dx** with identical FTIR as shown in Fig. S2 (ESI†). The solid-state ^{13}C NMR spectra (Fig. S3, ESI†) of the materials show broad multi-peaks between δ = 100 and 170 ppm. The peaks at 151 ppm for **H2-ICOP** and 152 ppm for **Zn-ICOP** can be attributed to the carbon signals in the bipyridinium moieties, whereas the peaks at 122 ppm for **H2-ICOP** and **Zn-ICOP** correspond to phenyl carbons of the porphyrin subunit.

The diffuse reflectance spectroscopy (DRS) of **H2-ICOP** and **Zn-ICOP** displays the characteristic Soret and Q bands of the porphyrin at 436 nm and 535 nm for **H2-ICOP**, and 447 nm and 538 nm for **Zn-ICOP** (Fig. 2a). Moreover, characteristics of viologen radical bands were observed at 627 nm for **H2-ICOP**

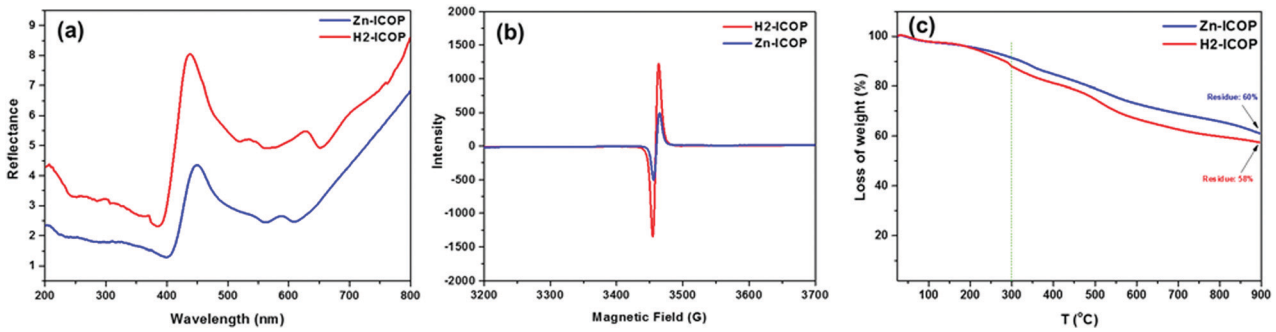

Fig. 2 DR spectra (a), EPR signals (b) and TGA curves (c) of **H2-ICOP** and **Zn-ICOP**.

and 586 nm for **Zn-ICOP**. **H2-ICOP** and **Zn-ICOP** exhibit an electron paramagnetic resonance (EPR) signal (Fig. 2b). The radical character of these ICOPs is the result of charge transfer from the aromatic porphyrin core to the viologen unit and is an indication of the highly conjugated structures.[57]

Thermogravimetric analysis (TGA) shows that **H2-ICOP** and **Zn-ICOP** exhibit thermal stability up to 300 °C with slight weight losses (Fig. 2c). However, it is noteworthy that both materials retain about 60% of their initial mass even at 900 °C, indicating good thermal stability. **H2-ICOP** and **Zn-ICOP** have similar experimental PXRD profiles with low angle diffraction peaks in the vicinity of 2θ values of 5°, which is characteristic for expected large unit-cell parameters (Fig. S4, ESI†). However, the broadening of peaks in both profiles in combination with a large peak at *ca.* 22.5° indicates a semi-crystalline nature of the studied materials. To determine the structures of **H2-ICOP** and **Zn-ICOP**, the geometry optimization of constructed models having the eclipsed (AA) and staggered (AB) topology was performed using the ABINIT code using the following unit cell parameters: $a = b = 35.563$, $c = 4.09$ (7.8 for the staggered structure) Å, $\alpha = \beta = \gamma = 90°$, space group *P*1. The comparisons of both the experimental and calculated PXRD profiles based on the relaxed models are presented in Fig. S4a for **H2-ICOP** and in Fig. S4b (ESI†) for **Zn-ICOP**. The experimental PXRD profiles of both ICOPs are in good agreement with the simulated staggered AB-stacking model (Fig. S4d, ESI†). Since the PXRD patterns of **H2-ICOP-dx** and **Zn-ICOP-dx** showed an amorphous nature rather than a semi-crystalline structure, **H2-ICOP** and **Zn-ICOP** were used for further investigations. Elemental mapping by energy dispersive spectroscopy (EDS) exhibits the elements C, N, and Cl for **H2-ICOP** and C, N, Cl, and Zn for **Zn-ICOP** (Fig. S5, ESI†), which is consistent with the compositions of our ICOPs. Dynamic light scattering (DLS) analyses showed two particle populations with an average colloidal particle size in the range between 1 and 10 μm for both ICOPs, suggesting a polydisperse nature (Fig. S6, ESI†). The stability of colloidal systems of **H2-ICOP** and **Zn-ICOP** was evaluated with zeta potential measurements in water (pH = 7.4) (Fig. S7, ESI†). Interestingly, the zeta potential of **H2-ICOP** shows a positive value (+25), whereas **Zn-ICOP** shows a negative zeta potential value (−21.6). These high absolute values of the zeta potential of **H2-ICOP** and **Zn-ICOP** indicate a stable state of their colloidal systems, which is also confirmed by observation of the Tyndall effect (Fig. S8, ESI†). Furthermore, the zeta potential data not only reflect the stability of the colloidal systems of **H2-ICOP** and **Zn-ICOP** dispersions in water but also can be used to explain the adsorption and conversion mechanisms of CO_2, which we will discuss in related sections.

Depending on the solvent mixture used, structures with different morphologies were obtained. Scanning electron microscopy (SEM) and transmission electron microscopy (TEM) studies reveal that the ICOPs obtained by using the DMF : water mixture (**H2-ICOP** and **Zn-ICOP**) exhibit a sheet-like morphology, whereas the ICOPs obtained by using the 1,4-dioxane : water mixture (**H2-ICOP-dx** and **Zn-ICOP-dx**) exhibit a spherical morphology (Fig. 3). Uniform spheres with an average diameter of 1.4 μm for **H2-ICOP-dx** and 0.65 μm for **Zn-ICOP-dx** were observed by both SEM (Fig. 3b and d and Fig. S9, ESI†) and TEM analysis (Fig. 3f and h).

2.2. CO_2 uptake and CO_2/N_2 selectivity performance

To investigate the permanent porosity of **H2-ICOP** and **Zn-ICOP**, krypton (Kr) adsorption–desorption isotherms were measured *via* the Brunauer–Emmett–Teller (BET) model, at 77 K (for details see the ESI†). As shown in Fig. 4b, both **H2-ICOP** and **Zn-ICOP** show typical type-II reversible adsorption isotherms and their porosities are found to be mesoporous in the range of 3–20 nm, whereas the nitrogen (N_2) adsorption–desorption isotherms show non-porous surfaces. The specific surface areas of **H2-ICOP** and **Zn-ICOP** were found to be 9 $m^2\ g^{-1}$ and 20 $m^2\ g^{-1}$, respectively (Fig. 4a). This difference in the BET surface areas can be explained by the zeta potential values of **H2-ICOP** (+25) and **Zn-ICOP** (−21.6) (Fig. S7, ESI†). The positive

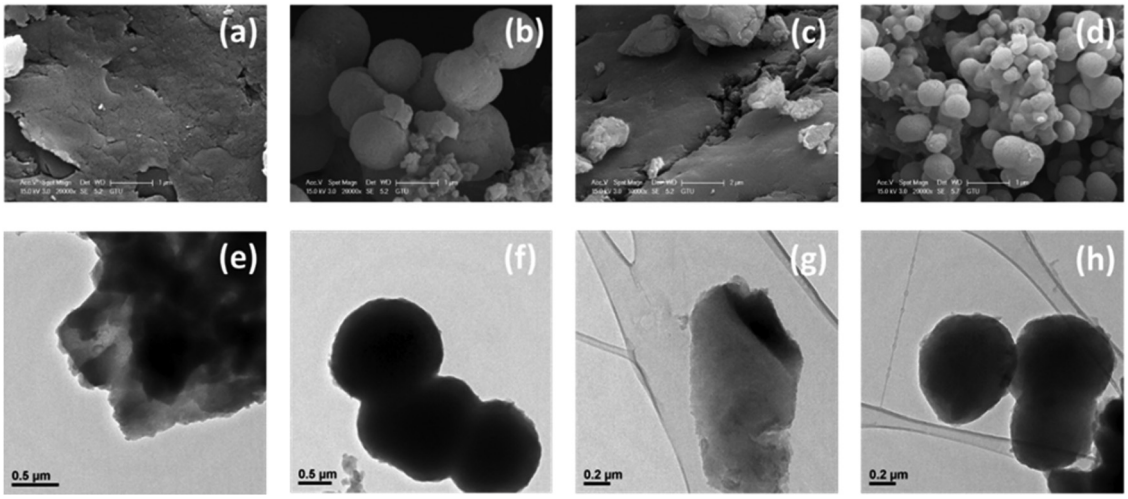

Fig. 3 Microscopic characterization [SEM (top row) and TEM (bottom row)] of **H2-ICOP** (a and e) and **Zn-ICOP** (c and g) prepared in DMF : water (4 : 1, v/v) and obtained as plates; and **H2-ICOP-dx** (b and f) and **Zn-ICOP-dx** (d and h) prepared in 1,4-dioxane : water (4 : 1, v/v) and obtained as spheres.

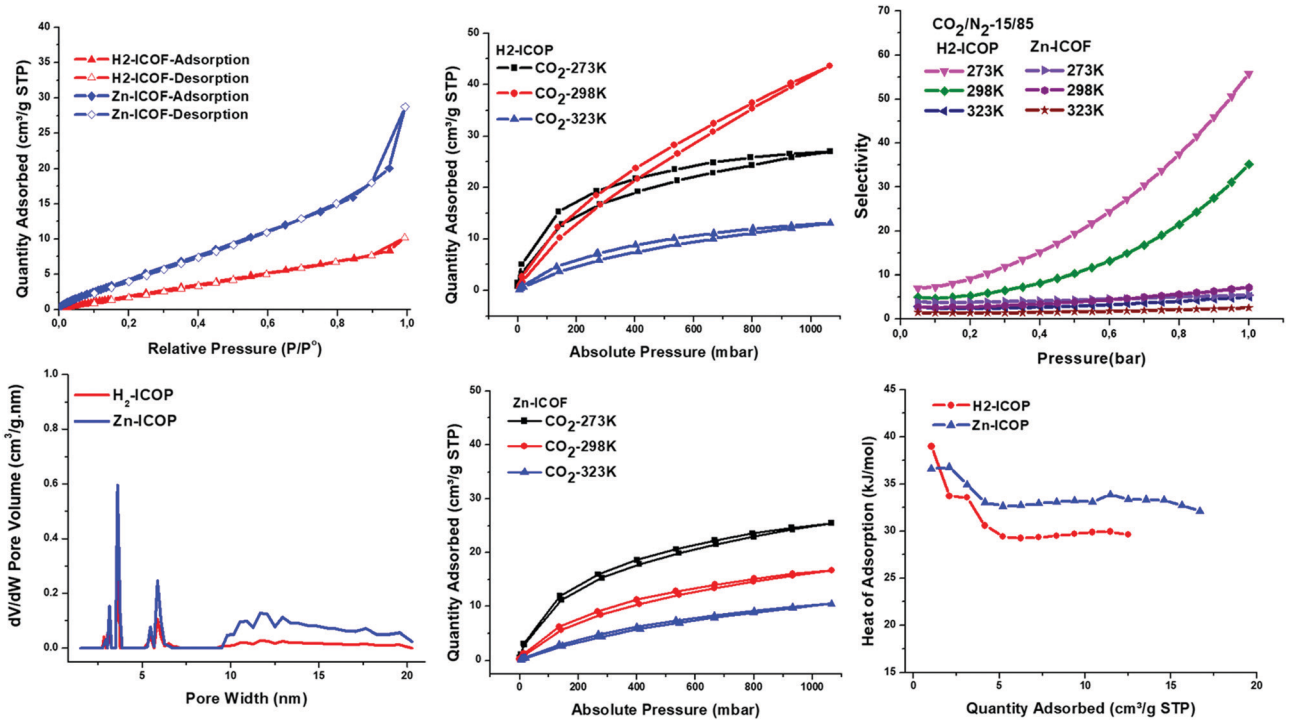

Fig. 4 (a) Kr adsoption/desorption isotherms of **H2-ICOP** and **Zn-ICOP** measured at 77 K, filled and empty symbols represent adsorption and desorption, respectively. (b) Pore size distribution of **H2-ICOP** and **Zn-ICOP** calculated from Kr isotherms calculated using NLDFT. CO_2 adsorption isotherms of **H2-ICOP** (c) and **Zn-ICOP** (d) collected up to 1 bar at 273, 298, and 323 K. (e) CO_2/N_2 (IAST method) selectivity of **H2-ICOP** and **Zn-ICOP** at 273 K, 298 K, and 323 K. (f) The isosteric heat of adsorption (Q_{st}) plots of CO_2 for **H2-ICOP** and **Zn-ICOP**.

zeta potential value suggests that the pores are occupied by nearly all of the chloride counter ions and they do not remain on the surface of **H2-ICOP**, whereas the negative zeta potential value indicates that some chloride counter-ions remain on the surface of **Zn-ICOP**. Notably, the surface areas of both ICOPs are one of the lowest values reported to date for any ICOP. These relatively low values are likely due to the pores of the materials being occupied by chloride counterions and their semi-crystalline state and staggered morphology with an AB stacking sequence (Fig. S4d, ESI†).

Owing to their multiple CO_2-philic sides, despite their low surface areas, we explored the affinity of **H2-ICOP** and **Zn-ICOP** toward CO_2 and N_2. To evaluate their performance for CO_2 capture, we carried out temperature-dependent CO_2 uptake measurements at 273, 298, and 323 K up to 1 bar (Fig. 4c and d). The CO_2 capture capacity of **H2-ICOP**, despite the lower BET surface area, is found to be up to 26 (42.4 mg g^{-1}, 273 K), 44 (62.9 mg g^{-1}, 298 K), and 13 cm^3 g^{-1} (17.3 mg g^{-1}, 323 K) at 1 bar, which is much higher than that of **Zn-ICOP**, 25 (39.3 mg g^{-1}, 273 K), 16.7 (24 mg g^{-1}, 298 K) and 10.2 cm^3 g^{-1} (13.9 mg g^{-1}, 323 K) at 1 bar, respectively. Notably, the CO_2 uptake capacities are not saturated for **H2-ICOP** within the pressure range, suggesting that the CO_2 uptake capacities can be further improved with increased pressure. Remarkably, the CO_2 capture capacities of **H2-ICOP** and **Zn-ICOP** are one of the highest values reported among previously reported viologen based ICOFs and ICOPs with much larger surface areas (Table 1). The CO_2 capture capacity of these viologen linked

Table 1 BET surface area, CO_2 uptake, selectivity, and heat adsorptions (Q_{st}) of the ICOPs

ICOP	BET surface area (m^2 g^{-1})	CO_2 adsorption (mg g^{-1})			CO_2/N_2 selectivity (15/85) (IAST) 1 bar		Q_{st} (kJ mol^{-1})	Pressure (bar)	Ref.
		273 K	298 K	323 K	273 K	298 K			
H2-ICOP	9	42.4	62.9	17.3	56.5	35	39	1	This work
Zn-ICOP	20	39.3	24	13.9	5.6	6.9	36	1	This work
PCP-Cl	755	101	61.4	—	34	—	28.5	1	39
V-PCIF-Cl	174	86.7	62.4	—	—	—	56.6	1	43
POV-V1	812	—	40.5	—	—	—	25	1.1	49
POV-V2	960	—	55.9	—	—	—	24	1.1	49
c-CTF-400	744	126	83	52	—	—	49	1	34
c-CTF-450	861	99	62	38	—	—	46	1	34
c-CTF-500	1247	133	80	47	—	—	43	1	34
SYSU-Zn@IL1	38	68	40	—	—	—	27.2	1	47

ICOFs and ICOPs is attributed mainly to tetrel bonding interactions between the counter anions and CO_2. However, as the positive zeta potential value of **H2-ICOP** shows that the pores are occupied by nearly all of the chloride counter ions and they do not remain on the surface, yet **H2-ICOP** has a very high CO_2 capture capacity, the results indicate that **H2-ICOP**, due to our molecular design, possesses much stronger non-covalent interactions with CO_2 than the counter anions.

To gain further insights from the non-covalent interactions between the materials and CO_2 molecules, the CO_2 isosteric heat of adsorption (Q_{st}) of **H2-ICOP** and **Zn-ICOP** was obtained with the Clausius–Clapeyron equation from the CO_2 uptake isotherms recorded (Fig. 4f). The Q_{st} values for CO_2 were found to be 39 and 36 kJ mol^{-1} for **H2-ICOP** and **Zn-ICOP**, respectively, at zero coverage. This difference of the Q_{st} value for the two polymers shows that the non-covalent interactions of the CO_2 molecules with the skeleton of **H2-ICOP** are more efficient than with **Zn-ICOP**, which may explain the higher CO_2 capture capacity of **H2-ICOP** compared to **Zn-ICOP**. It is also worth mentioning that the Q_{st} values of the polymers are moderate, not exceeding 50 kJ mol^{-1}, which implies that CO_2 is physically adsorbed by both **ICOPs** and the recyclability of the adsorbent at a low energy penalty.

Additionally, to assess the potential in separation of CO_2 from flue gas (>70% N_2), the adsorption selectivity of CO_2 over N_2 (15/85) of **H2-ICOP** and **Zn-ICOP** was calculated with Myers and Prausnitz's ideal adsorbed solution theory (IAST) at three different temperatures (273, 298, and 320 K) up to 1 bar (Fig. 4e and Table 1).[58] The selectivity of CO_2 from CO_2/N_2 (15/85) of **H2-ICOP** and **Zn-ICOP** is 55.7 and 5.5 at 273 K, 35.1 and 7.2 at 298 K, and 5.1 and 2.55 at 323 K, respectively. As expected, **H2-ICOP** exhibits much higher selectivity compared to **Zn-ICOP**, which also indicates powerful CO_2 affinity of **H2-ICOP**.

2.3. Computational analysis of non-covalent bonds

The high CO_2 capture and selectivity capacities of **H2-ICOP** and **Zn-ICOP**, despite their low surface areas, clearly show the powerful non-covalent interactions between CO_2 molecules and multiple CO_2-philic moieties of **H2-ICOP** and **Zn-ICOP**. Theoretical analyses (for details of the computational methodology see the ESI†) have been performed to get insights into the possible non-covalent interactions between CO_2 molecules and the surfaces of **H2-ICOP** and **Zn-ICOP**, and their contribution to the selective CO_2 uptake of these compounds.

To model the mentioned non-covalent interactions, the fragments **H2-ICOP** and **Zn-ICOP** were 'cut off' from the polymeric chains and the linkers were replaced by hydrogen atoms. **H2-ICOP** and **Zn-ICOP** contain two porphyrin cores, a chlorine counterion, and a positively charged viologen linker. The σ-hole formation on the surface of **H2-ICOP**, **Zn-ICOP**, and **CO_2** has been visualized using electrostatic potential maps (MEP) and the results are displayed in Fig. 5 along with the corresponding electrostatic potential values. The calculated MEP surfaces show that a maximum of positive potential (σ-hole) involves a region with the cationic viologen subunits and **Zn-ICOP** porphyrin core (Zn) as well as the carbon atom C_{CO_2}, which shows the Lewis acid

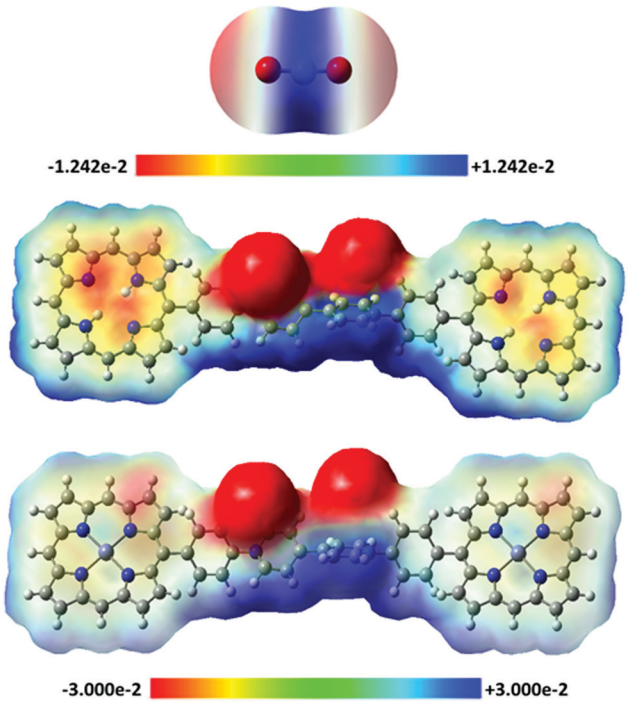

Fig. 5 Electrostatic potentials mapped on the molecular surfaces of CO_2, **H2-ICOP** and **Zn-ICOP**. The values of the MEPs lie in the intervals −7.794, +7.794 kcal mol^{-1} for CO_2 and −18.825, +18.825 kcal mol^{-1} for **H2-ICOP** and **Zn-ICOP**.

character of these regions. The negative electrostatic potential is located in the vicinity of oxygen O_{CO_2}, chlorine atoms, and nitrogen atoms in the **H2-ICOP** porphyrin core (Fig. 6). Thus, the positive and negative MEP distributions of **H2-ICOP**, **Zn-ICOP**, and **CO_2** indicate that attractive interactions are favourable for the formation of the above mentioned non-covalent bonds.

The MEP analyses have revealed possible non-covalent interactions, such as hydrogen, tetrel, pnicogen, and spodium bonds formed between CO_2 molecules and the surfaces of **H2-ICOP** and **Zn-ICOP**, and their contribution to the selective CO_2 uptake of these compounds (Fig. 6).

These noncovalent interactions can be uniformly defined based on the positive electrostatic region present on an atom due to the anisotropic distribution of the electron density. A positive electrostatic region present on an atom along a σ-polymer is called a σ-hole. The size and magnitude of a σ-hole are dependent on both the nature of its atom and the electron-withdrawing ability of groups

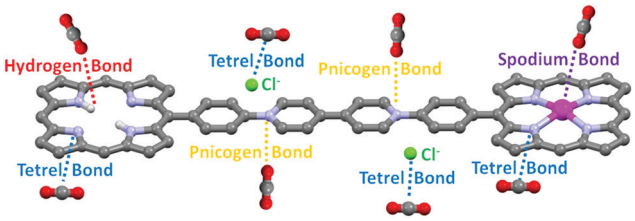

Fig. 6 Scheme of possible non-covalent interactions between CO_2 and **H2-ICOP** and **Zn-ICOP**.

attached to this atom. These σ-holes can have an attractive interaction with electron donors such as Lewis bases, anions or radicals. Depending on the σ-hole origins, these interactions are called tetrel bonding (group IV), pnicogen bonding (group V), chalcogen bonding (group VI), halogen bonding (group VII) or spodium bonding (group XII).[59]

Symmetry adapted perturbation theory (SAPT) analysis, which partitions the attractive forces into electrostatic (E_{elst}), exchange-repulsion (E_{exch}), induction (E_{ind}), and dispersion (E_{disp}) terms, has been carried out to calculate the interaction energy of hydrogen ($O_{CO_2}\cdots H$), tetrel ($C_{CO_2}\cdots N$, $C_{CO_2}\cdots Cl^-$), pnicogen ($O_{CO_2}\cdots N^+$), and spodium bonds ($O_{CO_2}\cdots Zn$) in **H2-ICOP** and **Zn-ICOP** and estimate the preferable binding sites to capture CO_2 molecules on their surfaces (Table 3). For all studied non-covalent interactions, the calculated attractive components E_{elst}, E_{ind}, and E_{disp} provide sufficient stabilization to overcome the repulsive exchange component E_{exch}, and the resultant interaction energy (E_{int}) values are negative, except hydrogen bonding. The value of E_{exch} for hydrogen bonds in **H2-ICOP** is very large and suppresses the other attractive components, and therefore the resulting interaction energy is positive, which indicates that the formation of H-bonds between CO_2 and –NH (porp) is not favourable (Table 2 and Fig. 7d). Dispersion forces (E_{disp}) are found to be dominant in the attractive binding energies of pnicogen ($O_{CO_2}\cdots N^+$) and $C_{CO_2}\cdots N$ tetrel bonds and spodium bonds ($O_{CO_2}\cdots Zn$), while electrostatic interactions (E_{elst}) dominate in $C_{CO_2}\cdots Cl^-$ tetrel bonds in both compounds. The percentage contribution of the dispersion term in the overall attractive forces for pnicogen bonds consists of 73% in **CO_2-H2-ICOP** and **CO_2-Zn-ICOP**, while for $C_{CO_2}\cdots N$ tetrel bonds in these systems it is equal to 58% and 66%, respectively. For spodium bonds the dispersion term constitutes 53%. For $C_{CO_2}\cdots Cl^-$ tetrel bonds in both compounds the percentage contribution of electrostatic interactions in the overall attractive forces consists of 58%.

Table 2 Summary of the SAPT results (kJ mol^{-1}) for pnicogen ($O_{CO_2}\cdots N^+$), tetrel ($C_{CO_2}\cdots N$, $C_{CO_2}\cdots Cl^-$), hydrogen ($H\cdots O_{CO_2}$) and spodium ($Zn\cdots O_{CO_2}$) bonds in **CO_2-H2-ICOP** and **CO_2-Zn-ICOP**. R is the bond length (Å)

Compound	LB···LA	Bond type	R	E_{elst}	E_{exch}	E_{ind}	E_{disp}	E_{int}
H2-ICOP	$O_{CO_2}\cdots N^+$	Pnicogen	3.115	−6.1	16.8	−2.0	−22.2	−13.6
	$Cl^-\cdots C_{CO_2}$	Tetrel	3.42	−16.3	11.0	−3.8	−7.9	−17.0
	$N\cdots C_{CO_2}$	Tetrel	2.976	−21.7	42.3	−5.5	−37.1	−22.0
	$O_{CO_2}{}^{a}\cdots H$	Hydrogen	1.961	−177.6	398.9	−21.2	−105.9	+94.3
Zn-ICOP	$O_{CO_2}\cdots N^+$	Pnicogen	3.115	−6.2	16.8	−2.0	−22.3	−13.7
	$Cl^-\cdots C_{CO_2}$	Tetrel	3.42	−16.4	11.0	−3.8	−7.9	−17.1
	$N\cdots C_{CO_2}$	Tetrel	2.976	−14.2	42.7	−5.2	−38.4	−15.2
	$O_{CO_2}\cdots Zn$	Spodium	2.6	−19.8	30.2	−5.8	−28.8	−21.1

[a] The D–H···A angles for both CO_2 are 125.8 and 118.7°.

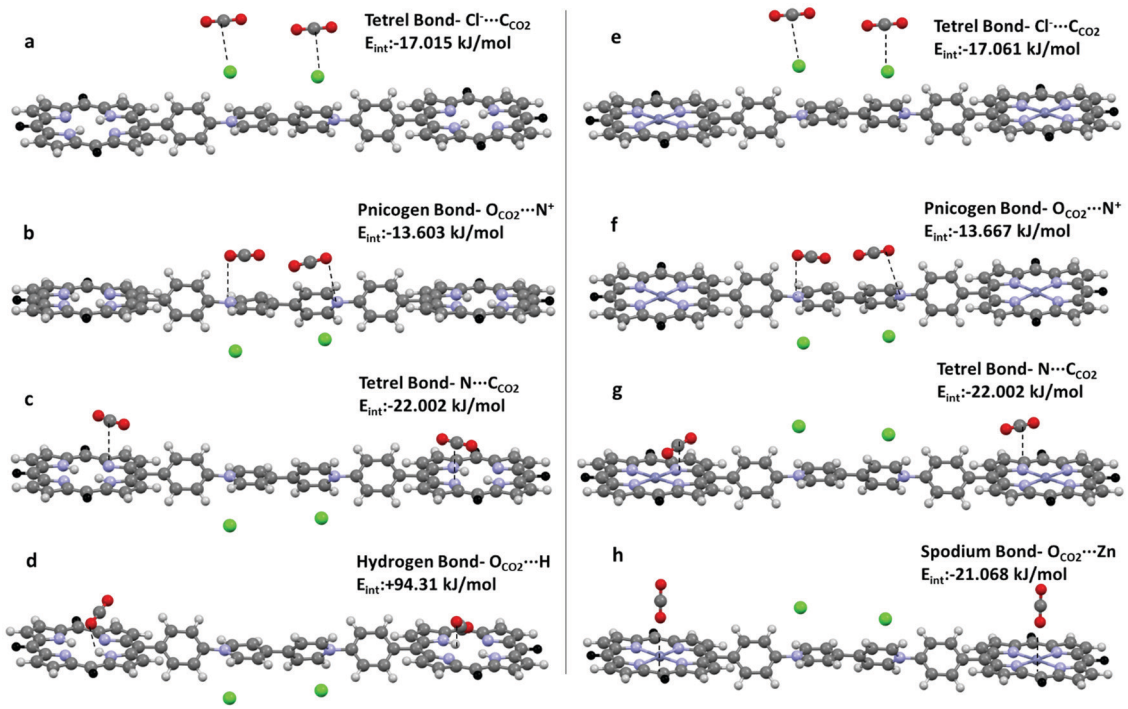

Fig. 7 Formation of (a, e, c and g) tetrel, (b and f) pnicogen, (d) hydrogen and (h) spodium bonds in **H2-ICOP** and **Zn-ICOP**.

The strength of the non-covalent interactions in **CO_2-H2-ICOP** and **CO_2-Zn-ICOP** is decreasing in the following order $\Delta E_{C\cdots N} > \Delta E_{C\cdots Cl^-} > \Delta E_{O\cdots N^+}$ and $\Delta E_{Zn\cdots O} > \Delta E_{C\cdots Cl^-} > \Delta E_{C\cdots N} > \Delta E_{O\cdots N^+}$, respectively (Table 2 and Fig. 7a–h). The binding energy of $C_{CO_2}\cdots N$ tetrel bonds in **CO_2-H2-ICOP** is -22.02 kJ mol^{-1} and is the strongest among the studied non-covalent interactions. Interestingly, upon Zn metalation in the porphyrin core, the binding energy of $C_{CO_2}\cdots N$ tetrel bonds in **CO_2-Zn-ICOP** is decreased to -15.163 kJ mol^{-1}, probably due to an increase of the positive electrostatic potential around nitrogen atoms (Fig. 6) in the porphyrin core, which resulted in the formation of weaker tetrel bonds ($C_{CO_2}\cdots N$) with CO_2. In addition, further analyses were performed to calculate the binding energy of the simultaneous presence, on the same porphyrin core, of two $C_{CO_2}\cdots N$ tetrel bonds in **H2-ICOP** and spodium and $C_{CO_2}\cdots N$ tetrel bonds in **Zn-ICOP**. The analyses reveal that the simultaneous presence of spodium and $C_{CO_2}\cdots N$ tetrel bonds is impossible on the same porphyrin core in **Zn-ICOP** because of the strong repulsion between two CO_2 molecules (Table S1 and Fig. S10, ESI†), while two tetrel bonds may form in the **H2-ICOP** porphyrin core because of negligible repulsion between CO_2 molecules (Fig. S11 and Table S1, ESI†). Overall, in our fragment model, **H2-ICOP** can potentially form two pnicogen, two $C_{CO_2}\cdots Cl^-$ and four $C_{CO_2}\cdots N$ tetrel bonds with CO_2, while **Zn-ICOP** can form two pnicogen, two $C_{CO_2}\cdots Cl^-$ tetrel, and two spodium bonds with CO_2. The major CO_2 uptake contribution comes from the four $C_{CO_2}\cdots N$ tetrel bonding interactions for **H2-ICOP**, whereas the two spodium bonding interactions for **Zn-ICOP**. In conclusion, **H2-ICOP** has more binding sites with more powerful non-covalent interactions that lead to an enhancement of the CO_2 uptake compared to **Zn-ICOP**, which is in good agreement with the experimental results.

2.4. The catalytic performance in CO_2 conversion into cyclic carbonates

To evaluate the catalytic activities of viologen-linked porphyrin **H2-ICOP** and **Zn-ICOP**, the cycloaddition of CO_2 to propylene oxide was chosen as a model reaction and the results are listed in Table 3. The reactions were conducted under 1.0 MPa CO_2 pressure and solvent and co-catalyst free conditions at 80 °C (for details see the ESI†).

The compared catalysts **Zn-ICOP** and **H2-ICOP** gave yields of 83% and 54%, respectively. Surprisingly, **Zn-ICOP**, despite having a significantly lower CO_2 uptake capacity, displayed better catalytic activity than **H2-ICOP**. The high activity of **Zn-ICOP** can be attributed to the synergistic effect of Lewis acid Zn sites and a nucleophile counter anion (Cl^-). The zeta potential data revealed that **Zn-ICOP** possesses a counter anion (Cl^-) on its surface, whereas **H2-ICOP** does not, which indicates the crucial role of the counter anion (Cl^-) in the mechanism of this catalytic reaction.[46,47] Notably, the catalytic activity of **Zn-ICOP** was achieved with lowered temperature and CO_2 pressure, in a solvent-free reaction system, and was comparable to that of most of the reported examples (Table 3).

The catalytic performance of **Zn-ICOP** was compared with that of the corresponding polymer SYSU-Zn@IL1(Br^-) since both structures are based on Zn–porphyrin and viologen. SYSU-Zn@IL1, with a BET surface area of 38 m^2 g^{-1}, has a nearly identical chemical composition to **Zn-ICOP**. Under similar conditions, **Zn-ICOP** had 83% conversion of PO, whereas SYSU-Zn@IL1(Br^-) could only afford a PO conversion of 62%. The higher activity of **Zn-ICOPz**(Cl^-) is mainly attributed to the higher nucleophilicity of its counter anions ($Cl^- > Br^-$).

Under the optimized reaction conditions, the catalytic activity of **Zn-ICOP** was further studied over a variety of epoxides. As shown in Table 4, various epoxides are efficiently converted into the desired products with moderate yields under mild conditions by **Zn-ICOP**. With the increase of the size of epoxides, a steady decrease in the yield of cyclic carbonates was observed from PO (83%) and 1,2-epoxybutane (42%) to styrene oxide (4%), likely owing to their increasing steric hindrance, except for epichlorohydrin (77%) (Table 4). The deviation of epichlorohydrin's yield from the trend, despite its larger size, is probably due to additional non-covalent interactions between the chlorine functional group and CO_2.

Table 3 The cycloaddition of CO_2 with propylene oxide (PO) catalysed by various ICOPs

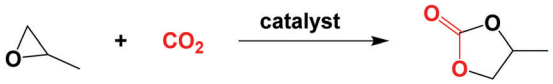

Catalyst	Loading	T (°C)	P_{CO_2} (bar)	t (h)	Yield (%)	Ref.
CTF-P-HSA	0.1 g	130	6.9	4	83	60
cCTF	4 wt%	90	10	12	99	34
PCP-Cl	5 wt%	100	30	12	99	39
Zn-CIF2-C_2H_5	0.18 mol%	120	25	5	98	61
TBB-Bpy-a	0.08 g	120	10	4	99	48
COF-salen-Zn	0.1 mol%	100	20	3	90	62
SYSU-Zn@IL1	0.16 mol%	80	10	12	62	47
H2-ICOP	0.16 mol%	80	10	12	54	[a]
Zn-ICOP	0.16 mol%	80	10	12	83	[a]

[a] This work (yields are determined by ^{1}H NMR).

Table 4 The addition of CO_2 to various epoxides by the **Zn-ICOP** catalyst. Reaction conditions: epoxide (1 mL), catalyst (0.16 mol%), 80 °C, 1 MPa, 12 h

Epoxide				
Product				
Conversion (%)	83	42	77	4

3. Conclusion

Two viologen-porphyrin based ionic covalent organic polymers were constructed by a one-pot facile Zincke reaction. The BET surface area analyses reveal that both **H2-ICOP** (9 m^2 g^{-1}) and **Zn-ICOP** (20 m^2 g^{-1}) possess a very low surface area. Yet, despite their nearly non-porous surfaces, especially **H2-ICOP**

exhibits a very large CO_2 capture capacity and CO_2/N_2 selectivity, which indicates efficient non-covalent interactions with CO_2. The theoretical analyses show that **H2-ICOP** can potentially form two pnicogen, two $C_{CO_2}\cdots Cl^-$ and four $C_{CO_2}\cdots N$ tetrel bonds with CO_2, while **Zn-ICOP** can form two pnicogen, two $C_{CO_2}\cdots Cl^-$ tetrel, and two spodium bonds with CO_2. The strength of the non-covalent interactions in **H2-ICOP** and **Zn-ICOP** is decreasing in the following order $\Delta E_{C\cdots N} > \Delta E_{C\cdots Cl^-} > \Delta E_{O\cdots N^+}$ and $\Delta E_{Zn\cdots O} > \Delta E_{C\cdots Cl^-} > \Delta E_{C\cdots N} > \Delta E_{O\cdots N^+}$, respectively. The binding energy of $C_{CO_2}\cdots N$ tetrel bonds in **CO_2-H2-ICOP** is -22.02 kJ mol^{-1} and is the strongest among the studied non-covalent interactions. The major CO_2 uptake contribution comes from the four $C_{CO_2}\cdots N$ tetrel bonding interactions for **H2-ICOP**, whereas the two spodium bonding interaction for **Zn-ICOP**. Furthermore, the CO_2 catalytic conversion performances of **Zn-ICOP** and **H2-ICOP** gave encouraging yields of 83% and 54%, respectively. Surprisingly, **Zn-ICOP**, even with a significantly lower CO_2 uptake capacity, displayed better catalytic activity than **H2-ICOP**, probably due to the crucial role of the counter anion (Cl^-) in the mechanism of this catalytic reaction.

Overall, we have demonstrated here that ICOPs with multiple CO_2-philic sites can indeed exhibit very large CO_2 capture capacity, CO_2/N_2 selectivity, and highly efficient catalytic activity of CO_2 cycloaddition of epoxides, owing to efficient non-covalent interactions with CO_2, in spite of low surface areas. These results set a useful example for the importance of non-covalent interactions with CO_2 for the capture and conversion of CO_2 into value-added products. Therefore, we believe that these findings will prove to be of key importance to the design of bifunctional charged materials for CCU applications.

Author contributions

The manuscript was written through contributions of all authors. All authors have given approval to the final version of the manuscript.

Conflicts of interest

There are no conflicts to declare.

Acknowledgements

The authors thank the TUBITAK ULAKBIM High Performance and Grid Computing Center (TRUBA resources), Turkey, for computational facilities. Y. Zorlu acknowledges financial support from The Science Academy, Young Scientist Award (BAGEP).

References

1 V. Scott, S. Gilfillan, N. Markusson, H. Chalmers and R. S. Haszeldine, *Nat. Clim. Change*, 2013, **3**, 105–111.
2 R. M. Cuéllar-Franca and A. Azapagic, *J. CO2 Util.*, 2015, **9**, 82–102.
3 A. Modak, P. Bhanja, S. Dutta, B. Chowdhury and A. Bhaumik, *Green Chem.*, 2020, **22**, 4002–4033.
4 C. Hepburn, E. Adlen, J. Beddington, E. A. Carter, S. Fuss, N. Mac Dowell, J. C. Minx, P. Smith and C. K. Williams, *Nature*, 2019, **575**, 87–97.
5 G. Singh, J. Lee, A. Karakoti, R. Bahadur, J. Yi, D. Zhao, K. Albahily and A. Vinu, *Chem. Soc. Rev.*, 2020, **49**, 4360–4404.
6 M. Bui, C. S. Adjiman, A. Bardow, E. J. Anthony, A. Boston, S. Brown, P. S. Fennell, S. Fuss, A. Galindo, L. A. Hackett, J. P. Hallett, H. J. Herzog, G. Jackson, J. Kemper, S. Krevor, G. C. Maitland, M. Matuszewski, I. S. Metcalfe, C. Petit, G. Puxty, J. Reimer, D. M. Reiner, E. S. Rubin, S. A. Scott, N. Shah, B. Smit, J. P. M. Trusler, P. Webley, J. Wilcox and N. Mac, Dowell, *Energy Environ. Sci.*, 2018, **11**, 1062–1176.
7 G. Sneddon, A. Greenaway and H. H. P. Yiu, The Potential Applications of Nanoporous Materials for the Adsorption, Separation, and Catalytic Conversion of Carbon Dioxide, *Adv. Energy Mater.*, 2014, **4**, 1301873–1301892.
8 A. A. Olajire, *J. CO2 Util.*, 2017, **17**, 137–161.
9 R. Dawson, E. Stöckel, J. R. Holst, D. J. Adams and A. I. Cooper, *Energy Environ. Sci.*, 2011, **4**, 4239–4245.
10 P. Bhanja, A. Modak and A. Bhaumik, *ChemCatChem*, 2019, **11**, 244–257.
11 W. Wang, M. Zhou and D. Yuan, *J. Mater. Chem. A*, 2017, **5**, 1334–1347.
12 H. A. Patel, J. Byun and C. T. Yavuz, *ChemSusChem*, 2017, **10**, 1303–1317.
13 R. Bera, M. Ansari, A. Alam and N. Das, *J. CO2 Util.*, 2018, **28**, 385–392.
14 M. Cox and R. Mokaya, *Sustainable Energy Fuels*, 2017, **1**, 1414–1424.
15 S. K. Shukla and J. P. Mikkola, *Phys. Chem. Chem. Phys.*, 2018, **20**, 24591–24601.
16 K. M. De Lange and J. R. Lane, *J. Chem. Phys.*, 2011, **135**, 0–8.
17 G. Chang, Z. Shang, T. Yu and L. Yang, *J. Mater. Chem. A*, 2016, **4**, 2517–2523.
18 M. Li, J. Lei, G. Feng, J. U. Grabow and Q. Gou, *Spectrochim. Acta, Part A*, 2020, **238**, 118424.
19 A. C. Legon, *Phys. Chem. Chem. Phys.*, 2017, **19**, 14884–14896.
20 X. Tan, L. Kou, H. A. Tahini and S. C. Smith, *Sci. Rep.*, 2015, **5**, 1–8.
21 D. Nam, P. De Luna, A. Rosas-hernández, A. Thevenon, F. Li, T. Agapie, J. C. Peters, O. Shekhah, M. Eddaoudi and E. H. Sargent, Molecular enhancement of heterogeneous CO_2 reduction, *Nat. Mater.*, 2020, **19**, 266–276.
22 B. Dash, *J. Mol. Model.*, 2018, **24**, 1–8.
23 P. Kanoo, R. Matsuda, H. Sato, L. Li, N. Hosono and S. Kitagawa, *Chem. – Eur. J.*, 2020, **26**, 2148–2153.
24 S. S. Rao and S. P. Gejji, *J. Phys. Chem. A*, 2016, **120**, 1243–1260.
25 L. M. Azofra and S. Scheiner, Tetrel, chalcogen, and CH···O hydrogen bonds in complexes pairing carbonylcontaining molecules with 1, 2, and 3 molecules of CO_2, *J. Chem. Phys.*, 2015, **142**, 034307-1–034307-9.
26 L. Lodeiro, R. Contreras and R. Ormazábal-Toledo, *J. Phys. Chem. B*, 2018, **122**, 7907–7914.
27 X. Y. Luo, X. Fan, G. L. Shi, H. R. Li and C. M. Wang, *J. Phys. Chem. B*, 2016, **120**, 2807–2813.
28 H. Y. Li, Y. X. Lu, X. Zhu, C. J. Peng, J. Hu, H. L. Liu and Y. Hu, *Sci. China: Chem.*, 2012, **55**, 1566–1572.

29 X. Zhu, Y. Lu, C. Peng, J. Hu, H. Liu and Y. Hu, *J. Phys. Chem. B*, 2011, **115**, 3949–3958.
30 V. Chernikova, O. Shekhah, Y. Belmabkhout and M. Eddaoudi, DOI: 10.1021/acsanm.0c00909.
31 S. K. Das, P. Bhanja, S. K. Kundu, S. Mondal and A. Bhaumik, *ACS Appl. Mater. Interfaces*, 2018, **10**, 23813–23824.
32 C. Liao, Z. Liang, B. Liu, H. Chen, X. Wang and H. Li, *ACS Appl. Nano Mater.*, 2020, **3**, 2889–2898.
33 Y. Fu, Z. Wang, S. Li, X. He, C. Pan, J. Yan and G. Yu, *ACS Appl. Mater. Interfaces*, 2018, **10**, 36002–36009.
34 O. Buyukcakir, S. H. Je, S. N. Talapaneni, D. Kim and A. Coskun, *ACS Appl. Mater. Interfaces*, 2017, **9**, 7209–7216.
35 Y. P. Zhao, Y. Li, C. Y. Cui, Y. Xiao, R. Li, S. H. Wang, F. K. Zheng and G. C. Guo, *Inorg. Chem.*, 2016, **55**, 7335–7340.
36 J. Wang, W. Sng, G. Yi and Y. Zhang, *Chem. Commun.*, 2015, **51**, 12076–12079.
37 A. E. Sadak, *Microporous Mesoporous Mater.*, 2021, **311**, 110727.
38 V. A. Online, M. M. Unterlass, F. Emmerling, M. Antonietti and J. Weber, From dense monomer salt crystals to CO_2 selective microporous polyimides *via* solid-state polymerization, *Chem. Commun.*, 2014, **50**, 430–432.
39 O. Buyukcakir, S. H. Je, D. S. Choi, S. N. Talapaneni, Y. Seo, Y. Jung, K. Polychronopoulou and A. Coskun, *Chem. Commun.*, 2016, **52**, 934–937.
40 J. Ding, C. Zheng, L. Wang, C. Lu, B. Zhang, Y. Chen, M. Li, G. Zhai and X. Zhuang, *J. Mater. Chem. A*, 2019, **7**, 23337–23360.
41 C. Hua, B. Chan, A. Rawal, F. Tuna, D. Collison, J. M. Hook and D. M. D'Alessandro, *J. Mater. Chem. C*, 2016, **4**, 2535–2544.
42 W. Hui, X. M. He, X. Y. Xu, Y. M. Chen, Y. Zhou, Z. M. Li, L. Zhang and D. J. Tao, *J. CO2 Util.*, 2020, **36**, 169–176.
43 G. Chen, X. Huang, Y. Zhang, M. Sun, J. Shen, R. Huang, M. Tong, Z. Long and X. Wang, *Chem. Commun.*, 2018, **54**, 12174–12177.
44 Y. Zhang, K. Zhang, L. Wu, K. Liu, R. Huang, Z. Long, M. Tong and G. Chen, *RSC Adv.*, 2020, **10**, 3606–3614.
45 T. Škorjanc, D. Shetty, M. A. Olson and A. Trabolsi, *ACS Appl. Mater. Interfaces*, 2019, **11**, 6705–6716.
46 Y. Zhang, K. Liu, L. Wu, H. Zhong, N. Luo, Y. Zhu, M. Tong, Z. Long and G. Chen, *ACS Sustainable Chem. Eng.*, 2019, **7**, 16907–16916.
47 Y. Chen, R. Luo, Q. Xu, J. Jiang, X. Zhou and H. Ji, *ACS Sustainable Chem. Eng.*, 2018, **6**, 1074–1082.
48 Y. Leng, D. Lu, P. Jiang, C. Zhang, J. Zhao and W. Zhang, *Catal. Commun.*, 2016, **74**, 99–103.
49 C. Hua, B. Chan, A. Rawal, F. Tuna, D. Collison, J. M. Hook and D. M. D'Alessandro, *J. Mater. Chem. C*, 2016, **4**, 2535–2544.
50 T. Lu, J. Zhang, Q. Gou and G. Feng, *Phys. Chem. Chem. Phys.*, 2020, **22**, 8467–8475.
51 S. J. Grabowski, *Struct. Chem.*, 2019, **30**, 1141–1152.
52 T. Skorjanc, D. Shetty, F. Gándara, L. Ali, J. Raya, G. Das, M. A. Olson and A. Trabolsi, *Chem. Sci.*, 2020, **11**, 845–850.
53 A. Bauzá, I. Alkorta, J. Elguero, T. J. Mooibroek and A. Frontera, *Angew. Chem.*, 2020, **132**, 17635–17640.
54 N. Manoranjan, D. H. Won, J. Kim and S. I. Woo, *J. CO2 Util.*, 2016, **16**, 486–491.
55 S. Zahedi and E. Safaei, *J. CO2 Util.*, 2020, **42**, 101308.
56 X. Jiang, F. Gou, X. Fu and H. Jing, *J. CO2 Util.*, 2016, **16**, 264–271.
57 G. Das, T. Skorjanc, S. K. Sharma, F. Gándara, M. Lusi, D. S. Shankar Rao, S. Vimala, S. Krishna Prasad, J. Raya, D. S. Han, R. Jagannathan, J. C. Olsen and A. Trabolsi, *J. Am. Chem. Soc.*, 2017, **139**, 9558–9565.
58 A. L. Myers and J. M. Prausnitz, *AlChE J.*, 1965, **11**, 121–127.
59 R. Parajuli, *Curr. Sci.*, 2016, **110**, 495–498.
60 J. Roeser, K. Kailasam and A. Thomas, *ChemSusChem*, 2012, **5**, 1793–1799.
61 J. Liu, G. Zhao, O. Cheung, L. Jia, Z. Sun and S. Zhang, *Chem. – Eur. J.*, 2019, **25**, 9052–9059.
62 H. Li, X. Feng, P. Shao, J. Chen, C. Li, S. Jayakumar and Q. Yang, *J. Mater. Chem. A*, 2019, **7**, 5482–5492.